HHS Public Access

Author manuscript

Magn Reson Med. Author manuscript; available in PMC 2022 August 01.

Published in final edited form as:

Magn Reson Med. 2021 August ; 86(2): 1067–1076. doi:10.1002/mrm.28776.

Synchrotron x-ray microcomputed tomography as a validation dataset for diffusion MRI in whole mouse brain

Scott Trinkle[1], **Sean Foxley**[1], **Narayanan Kasthuri**[2], **Patrick La Rivière**[1]

[1]Department of Radiology, University of Chicago, Chicago, IL, USA

[2]Department of Neurobiology, University of Chicago, Chicago, IL, USA

Abstract

Purpose: To introduce synchrotron x-ray microcomputed tomography (microCT) and demonstrate its use as as a natively isotropic, nondestructive, 3D validation modality for diffusion MRI (dMRI) in whole, fixed mouse brain.

Methods: Postmortem dMRI and microCT data were acquired of the same whole mouse brain. Diffusion data were processed using constrained spherical deconvolution. Synchrotron data were acquired at an isotropic voxel size of 1.17 μm. Structure tensor analysis was used to calculate fiber orientation distribution functions (fODFs) from the microCT data. A pipeline was developed to spatially register the two datasets in order to perform qualitative comparisons of fiber geometries represented by fODFs. Fiber orientations from both modalities were used to perform whole-brain deterministic tractography to demonstrate validation of long-range white matter pathways.

Results: fODFs were able to be extracted throughout the entire microCT dataset, with spatial registration to dMRI simplified due to the whole brain extent of the microCT data. Fiber orientations and tract pathways showed good agreement between modalities.

Conclusion: Synchrotron microCT is a potentially valuable new tool for future multi-scale dMRI validation studies, providing comparable value to optical histology validation methods while addressing some key limitations in data acquisition and ease of processing.

Keywords

diffusion MRI; microCT; validation; fiber orientation distribution function; whole mouse brain imaging; microstructure

1 Introduction

Diffusion magnetic resonance imaging (dMRI) is a method that estimates microanatomical tissue properties from macroscopic, spatio-angular measurements of the restricted diffusion of water molecules (1,2). Several dMRI acquisition and modeling approaches have been developed to estimate tissue properties such as fiber integrity (3,4), cellular compartmental analysis (5–7), axon diameters (8,9), and long-range fiber trajectories (10). Metrics derived

Correspondence: Scott Trinkle, Department of Radiology, University of Chicago, 5841 South Maryland Avenue, MC2026, Chicago, IL, 60637, trinkle@uchicago.edu.

from dMRI reconstructions have played an important role in the clinical diagnosis of several neurological diseases (11) but are limited by the poor spatial resolution of the data. Axons have diameters on the order of microns (12), while typical clinical dMRI voxels are on the order of millimeters. This discrepancy in scale introduces uncertainties in the reconstruction of microstructural tissue properties and long-range fiber pathways. Accordingly, dMRI methods require validation with ground-truth imaging across spatial scales capable of resolving micron-level cellular architectures as well as centimeter-level pathways and measures of connectivity across whole brains.

Efforts to validate dMRI reconstructions have primarily relied on optical imaging techniques. For the validation of local fiber orientation and dispersion properties estimated from dMRI, several groups have used histological analysis of tissue sections (13–17), polarized light imaging (18,19) and optical coherence tomography (20,21). Optical imaging methods have also been combined with fluorescent neural tracers to validate tractography pipelines in a number of species (22–26).

While optical imaging methods provide sufficient detail to characterize tissue microstructure and delineate white matter pathways, they also come with a number of limitations. The low penetration depth of optical light requires the tissue to be physically sectioned into thin slices. Three-dimensional (3D) representations of the sample are generated either by virtual stacking of two-dimensional images of each slice (27) or through deconvolution methods with confocal acquisitions (17,28). In both cases, the slice thickness is generally several times greater than the achievable in-plane resolution, leading to anisotropic voxel sizes. This effect can potentially bias the estimation of 3D fiber orientations and complicate the process of spatially registering the ground-truth and dMRI datasets. Optical acquisitions can also be prohibitively labor-intensive to deliver sufficient volumetric data across whole brains, requiring a method of preselecting target regions for imaging. Neural tracer studies are similarly limited to imaging projections to or from a single injection region per specimen, making ground-truth, whole-brain connectivity studies extremely costly.

Recent work has shown the ability to acquire micron-resolution synchrotron computed tomography (microCT) scans of the whole mouse brain and register them with both prior whole-brain dMRI and subsequent region-of-interest electron microscopy (EM) data (29). In this work, we present qualitative results demonstrating that this imaging pipeline can provide an alternative, complementary ground-truth dataset for dMRI validation. Synchrotron microCT addresses the limitations of optical imaging by providing isotropic, micron-level spatial resolution across whole mouse brains with no physical sectioning, allowing for future studies validating dMRI methods at the scale of local microstructural features up to long-range white matter pathways.

2 Methods

2.1 Animal procedures and tissue preparation

All procedures performed on animals followed protocols approved by the Institutional Animal Care and Use Committee. An eight-week-old, female C57BL/6 mouse (26 g) was anesthetized with 60 mg/kg pentobarbital. The animal was then injected with heparin

intraperitoneally and sacrificed by intercardial perfusion with 0.01 M phosphate buffer saline solution. This was immediately followed by 4% paraformaldehyde (pH 7.4)/PBS fixative solution. The brain was extracted from the skull and post-fixed in the same fixative overnight at 4°C and washed in PBS for 74 hours to remove fixative before imaging.

2.2 MRI acquisition and analysis

Prior to MRI experiments, the brain was submerged in Fluorinert (FC-3283, 3M Electronics) to improve shimming and mitigate susceptibility-mismatch artifacts. Data were acquired at 9.4 Tesla (20 cm internal diameter, horizontal bore, Bruker BioSpec Small Animal MR System, Bruker Biospin, Billerica, MA) using a 6 cm performance gradient insert (maximum gradient strength: 1000 mT/m, Bruker Biospin) and a 35 mm internal diameter quadrature volume coil (Rapid MR International, Columbus, Ohio). Diffusion data were acquired with a conventional 3D spin-echo/Stejskal-Tanner diffusion-weighted sequence at 150 μm isotropic resolution across 30 diffusion-encoding directions at a b-value of 3000 s/mm^2 (TR=400 ms, TE=18.5 ms, δ=5 ms, Δ=11.04 ms, receiver bandwidth=200 kHz, partial Fourier along first phase encoding direction=7/8, number b0s=10, duration=55 h 19 min 40 sec).

Before further analysis, the data were denoised using the dwidenoise protocol in the MRTrix3 software package (30–32). Fiber orientation distribution functions (fODFs) were calculated using constrained spherical deconvolution (33,34) up to a maximum spherical harmonic (SH) order of $\ell_{max} = 4$. The data were also fit to a tensor model (36) in order to calculate fractional anisotropy (FA) (1).

For anatomical reference, a water peak-height image was constructed from 3D echo-planar spectroscopic imaging (EPSI) of the same sample. This technique has been shown to be a high-fidelity T2*-weighted source of image contrast (37) and is particularly sensitive to local susceptibility changes associated with the presence of myelin in white matter (38). Data were acquired at 50 μm isotropic resolution using a multi-gradient echo sequence with an oscillating readout gradient train (TR=1000 ms, TE of first echo=3.41 ms, echo spacing=3.41 ms, number of echoes=128, receiver bandwidth=100 kHz, flip angle=84.3°, 4 averages, duration=21 h 23 min 44 s).

2.3 Synchrotron x-ray microCT acquisition

The sample preparation and data acquisition protocol used for microCT imaging has been recently published (29) and is briefly summarized here. Following dMRI acquisition, the brain was stained using the brain-wide reduced-osmium staining pyrogallol-mediated amplification protocol (39,40). MicroCT data were acquired at the sector 32-ID beamline of the Advanced Photon Source at Argonne National Laboratory with a central beam energy of 25.5 keV. Raw projection data had a field of view of 2.25×1.41 mm^2. A 6×18 grid of such acquisitions was collected to cover a total field of view sufficient to image the whole brain rotated around its rostral-caudal axis. This process was repeated across 3600 rotation angles. The projections were digitally aligned and stitched together using a mosaic tomography technique (41) and reconstructed into a single volume with an isotropic voxel size of 1.17 μm using the TomoPy package (42). Our microCT data can be viewed online through

Neuroglancer (http://neuroglancer-demo.appspot.com/) using http://nova.kasthurilab.com:8000/neuroglancer/recon_crop8_neurog/image as the precomputed source link.

2.4 Calculation of microCT fODFs

Voxel-wise fiber orientations were estimated throughout the microCT data using an image processing technique used in previous validation studies (13–17) called structure tensor analysis (43). This method uses image gradients to provide a 3D orientation estimate and a scalar confidence metric at every voxel. Voxels representing non-fiber tissue were excluded using thresholds on the confidence metric and the raw grayscale value (see Supporting Information for details). To construct fODFs, the dataset was subdivided into regions of interest (ROIs) matching the size of the corresponding dMRI voxels (150 μm). Within each ROI, histograms of fiber orientation estimates were fit to SH functions up to $\ell_{max} = 8$.

2.5 Spatial registration

Compared to optical techniques, registration of the microCT and dMRI datasets was simplified by the fact that unsectioned ground-truth data and fODFs were available across the whole brain, meaning that existing whole-brain registration routines could be applied directly. An overview of the registration pipeline is shown in Figure 1. The strategy was to calculate the transformation from microCT space to dMRI space by leveraging the anatomical detail of the EPSI peak-height image, then to apply this transformation to the microCT fODFs. First, the b0 images of the dMRI dataset were averaged to form a template. The EPSI volume was registered to the b0 template using an affine transformation calculated with the ANTS registration package (44,45). The microCT data were downsampled to dMRI resolution using the same binning ROIs used for fODF construction. Downsampled microCT data were then registered to the EPSI volume using affine and symmetric diffeomorphic transformations calculated using the SyN algorithm (46) in ANTs. The concatenated transforms from microCT to EPSI to b0 were then applied to the microCT fODFs using the mrtransform command in MRtrix3, which reorients (47) and modulates (48) fODFs to preserve fiber densities across bundles before and after transformation.

2.6 Tractography

Whole-brain deterministic tractography was performed with the SD_STREAM algorithm (30) in MRTrix3 using registered fODFs for each dataset to demonstrate the utility of microCT for long-range connectivity studies. A total of 200,000 streamlines were generated from each modality, with a step size of 37.5 μm and a maximum angle between successive steps of 35°.

3 Results

3.1 MicroCT fODFs

Structure tensor analysis was used to calculate a total of n=151,094 fODFs from the microCT data, requiring around 120 hours of computation using 128 cores of a local computing cluster. Figure 2 shows representative axial slices of microCT data, with insets visualizing fODFs as 3D glyphs. Squares in the 3×3 grids within each inset represent ROIs

the size of a single dMRI voxel. The fODFs agree qualitatively very well with the fiber orientations observed in the microCT data, closely following the arc in the anterior commissure (yellow) and corpus callosum (red), capturing the parallel fibers of the posterior (blue) and anterior (pink) commissures, and the change in fiber orientations where the lateral septal complex of the striatum intersects the fornix system (green).

The size of the microCT fODFs is proportional to the fraction of voxels within each ROI identified as representing fibers. This is clearly seen along the anterior commissure (Figure 2, pink): the fODFs calculated within fiber-dense ROIs are much larger than those outside the main tract. This fraction can be considered a proxy for fiber density (FD), and is visualized in Figure 3. The FD metric shows good contrast between gray and white matter, indicating that the structure-tensor pipeline was successful in correctly identifying white matter fibers.

3.2 Spatial correspondence of fODFs

An example of registered microCT fODFs is shown across a slice of downsampled microCT data in Figure 4 alongside the corresponding dMRI fODFs. The two modalities show good qualitative correspondence in anatomical structures and fODF shapes, particularly along the fiber pathways shown in the inset. Full registration results are visualized in Supporting Information Video S1.

3.3 Tractography

Deterministic tractography was used to map long-range white matter pathways across both datasets. Whole-brain tractography results are shown in Figure 5. Overall, tracts from the two modalities show good visual agreement in the mapping of major tracts, indicating the success of dMRI tractography algorithms on structure tensor-derived fODFs, further demonstrating the multi-modal correspondence in fiber orientation information and motivating the use of microCT in future connectivity and tractography validation studies.

4 Discussion

Full characterization of the strengths and weaknesses of various dMRI methods will require the application of several complementary ground-truth imaging approaches. This study set out to introduce and qualitatively probe the capabilities of whole-brain synchrotron x-ray microCT as a new approach that specifically addresses some limitations in optical-based techniques. Note that we chose to forego efforts to quantitatively evaluate dMRI performance due to the relatively poor angular resolution of the dMRI data collected for this study. Our data were acquired with only 30 diffusion directions which were found after acquisition to be non-uniformly spaced across the sphere (Supporting Information Figure S1) due to a software malfunction. Accordingly, we chose to limit reconstructions to $\ell = 4$ (15 coefficients) to provide robustness to noise. For this reason, our goal was to introduce microCT and show meaningful, qualitative correspondence between reconstructions from the two modalities, rather than draw conclusions on the performance of any specific dMRI method. To that end, we are encouraged by the level of multi-modal correlation seen in the

fODFs (Figures 4–5) and believe it demonstrates the utility of synchrotron microCT for future validation studies.

4.1 Comparison of microCT with optical methods

Optical imaging techniques achieve in-plane resolutions on the order of hundreds of nanometers. For volumetric acquisitions, however, the through-plane resolution is significantly higher, dictated by slice thicknesses on the order of tens of microns and the limits of deconvolution methods. Accordingly, while in-plane optical images are sufficient for resolving individual axons and other details of neural microstructure, the limited through-plane resolution and geometric corrections required after tissue sectioning complicate the reconstruction of large volumes and might bias the estimation of features relevant to dMRI validation, such as fiber orientations. The microCT data used in this study has a nominal resolution of 1.17 μm. While this is lower than achievable optical resolutions, our results show that it is sufficient for resolving the orientation of local fiber bundles (Figure 2). Importantly, the data have natively isotropic resolution, avoiding the need for extensive post-processing to estimate the 3D architecture of the neural tissue.

Limitations on feasible data acquisition times and storage have required previous optical-based validation studies to preselect specific ROIs for high-resolution imaging, based on prior anatomical knowledge (17) or automated, data-driven approaches (21). Alternatively, synchrotrons provide enough x-ray flux to image the entire mouse brain with sufficient signal-to-noise ratio in a single day of acquisition. This provides more data for each specimen and removes potential user bias in the selection of regions for validation.

Optical imaging methods rely on neural tracer injections to map long-range fiber pathways for tractography validation. These methods provide unparalleled specificity at the cost of only allowing one injection per dataset, which prohibits validation of whole connectomes in individual specimens. We have shown in previous work (29) the potential for direct tracing of individual axons in synchrotron microCT datasets without the need for neural tracers. This direct approach is not feasible with standard optical methods, as slice cutting and mounting are associated with tissue distortions (50) that make it prohibitively challenging to reliably trace axons across slice boundaries after digital alignment.

This work also demonstrates that volumetric imaging of whole samples with microCT greatly eases spatial registration between modalities (Figures 1 and 4). Optical-based validation studies have typically depended on complicated, multi-step registration pipelines involving multiple histological acquisitions at different scales to map individual histological ROIs to the corresponding dMRI voxels (17,21). With isotropic resolution across the whole brain, microCT data can be registered directly to MRI using existing packages after appropriate downsampling.

4.2 Future work and limitations

While this study was limited to data from a single specimen, we believe our qualitative results are promising and motivate the collection of additional data for future quantitative dMRI validation studies. Various fODF reconstruction methods will be benchmarked against microCT at different spatial scales, evaluating agreement in fODF shape, peak identification,

and fiber dispersion metrics. Discrepancies between modalities will be further explored at the nanoscale using the volumetric EM imaging capabilities of our full imaging pipeline (29).

The tractography results presented in this study (Figure 5) suggest an additional benefit of large-volume microCT. With fODFs available across the whole brain, ground-truth tractography can be correlated with axon tracings and dMRI tractography at different scales in the same specimen. Such a rich dataset could be used in future studies to better understand the upper bounds of tractography performance and to explore new priors to better condition the tractography problem.

While we believe microCT is a valuable tool for dMRI validation, it also presents some limitations. Fiber orientation estimation can be biased by ring artifacts in the reconstructed data, caused by drifting fluctuations in the synchrotron beam which lead to inaccurate intensity normalization. Several successful algorithms exist to mitigate this artifact (51–53). Implementation of these approaches was outside the scope of this work but will be important for future future studies.

MicroCT is also limited by the achievable field of view and resolution. The narrow beam width necessitates the use of mosaic tomography for imaging large volumes. The computational challenge of precise sinogram registration currently limits achievable voxel sizes to around one micron, biasing orientation estimates towards fibers of this length scale. With limitations on feasible stain penetration depth, whole mouse brains represent an upper limit of volumes that can be imaged with this method. This prohibits the use of microCT for whole-brain studies of larger species, though smaller brain volumes from these species can still deliver valuable information.

5 Conclusion

A processing pipeline was developed for dMRI validation with synchrotron microCT. MicroCT provides isotropic resolution across whole mouse brains with no physical sectioning, addressing limitations in optical-based dMRI validation methods. Fiber orientations were estimated, processed into fODFs, and spatially registered to dMRI data from the same specimen. Comparisons between modalities show good agreement in the represention of local fiber geometries and the mapping of long-range fiber trajectories, movitating the use of microCT for future dMRI validation studies.

Supplementary Material

Refer to Web version on PubMed Central for supplementary material.

Acknowledgments

S.T. is supported by the National Institutes of Health (NIH) (F31NS113571). N.K. is supported by the NIH Brain Initiative (U01MH109100). P.L.R. is partially supported by the NIH (R01EB026300). Additional funding was provided by the NIH (S10OD025081, S10RR021039, P30CA14599). This research used resources of the Advanced Photon Source, a U.S. Department of Energy (DOE) Office of Science User Facility operated for the DOE Office of Science by Argonne National Laboratory: Contract No. DE-AC02-06CH11357.

References

1. Basser PJ, Pierpaoli C. Microstructural and Physiological Features of Tissues Elucidated by Quantitative-Diffusion-Tensor MRI. Journal of Magnetic Resonance, Series B 1996;111:209– 219. [PubMed: 8661285]
2. Novikov DS, Fieremans E, Jespersen SN, Kiselev VG. Quantifying brain microstructure with diffusion MRI: Theory and parameter estimation. NMR in Biomedicine. 2019;32:e3998. [PubMed: 30321478]
3. Fieremans E, Novikov DS, Jensen JH, Helpern JA. Monte Carlo study of a two-compartment exchange model of diffusion. NMR in Biomedicine. 2010;23:711–724. [PubMed: 20882537]
4. Fieremans E, Jensen JH, Helpern JA. White matter characterization with diffusional kurtosis imaging. NeuroImage. 2011;58:177–188. [PubMed: 21699989]
5. Kroenke CD, Ackerman JJ, Yablonskiy DA. On the nature of the NAA diffusion attenuated MR signal in the central nervous system. Magnetic Resonance in Medicine. 2004;52:1052–1059. [PubMed: 15508157]
6. Jespersen SN, Kroenke CD, Østergaard L, Ackerman JJ, Yablonskiy DA. Modeling dendrite density from magnetic resonance diffusion measurements. NeuroImage. 2007;34:1473–1486. [PubMed: 17188901]
7. Zhang H, Schneider T, Wheeler-Kingshott CA, Alexander DC. NODDI: Practical in vivo neurite orientation dispersion and density imaging of the human brain. NeuroImage. 2012;61:1000–1016. [PubMed: 22484410]
8. Assaf Y, Blumenfeld-Katzir T, Yovel Y, Basser PJ. AxCaliber: a method for measuring axon diameter distribution from diffusion MRI. Magnetic resonance in medicine. 2008;59:1347–1354. [PubMed: 18506799]
9. Alexander DC, Hubbard PL, Hall MG, et al. Orientationally invariant indices of axon diameter and density from diffusion MRI. NeuroImage. 2010;52:1374–1389. [PubMed: 20580932]
10. Jeurissen B, Descoteaux M, Mori S, Leemans A. Diffusion MRI fiber tractography of the brain. NMR in Biomedicine. 2019;32:e3785. [PubMed: 28945294]
11. Tae WS, Byung-Joo H, Sung-bom P, Kang SH, Kim BJ. Current Clinical Applications of Diffusion-Tensor Imaging. Journal of Clinical Neurology. 2018;14:129–140. [PubMed: 29504292]
12. Liewald D, Miller R, Logothetis N, Wagner HJ, Schüz A. Distribution of axon diameters in cortical white matter: an electron-microscopic study on three human brains and a macaque. Biological Cybernetics. 2014;108:541–557. [PubMed: 25142940]
13. Budde MD, Frank JA. Examining brain microstructure using structure tensor analysis of histological sections. NeuroImage. 2012;63:1–10. [PubMed: 22759994]
14. Budde MD, Annese J. Quantification of anisotropy and fiber orientation in human brain histological sections. Frontiers in Integrative Neuroscience. 2013;7:1–8. [PubMed: 23355815]
15. Khan AR, Cornea A, Leigland LA, Kohama SG, Jespersen SN, Kroenke CD. 3D structure tensor analysis of light microscopy data for validating diffusion MRI. NeuroImage. 2015;111:192–203. [PubMed: 25665963]
16. Seehaus A, Roebroeck A, Bastiani M, et al. Histological validation of high-resolution DTI in human post mortem tissue. Frontiers in Neuroanatomy. 2015;9:1–12. [PubMed: 25657619]
17. Schilling KG, Janve V, Gao Y, Stepniewska I, Landman BA, Anderson AW. Histological validation of diffusion MRI fiber orientation distributions and dispersion. NeuroImage. 2018;165:200–221. [PubMed: 29074279]
18. Axer M, Strohmer S, Gräßel D, et al. Estimating Fiber Orientation Distribution Functions in 3D-Polarized Light Imaging. Frontiers in Neuroanatomy. 2016;10:1–12. [PubMed: 26834571]
19. Mollink J, Kleinnijenhuis M, Cappellen van Walsum AM, et al. Evaluating fibre orientation dispersion in white matter: Comparison of diffusion MRI, histology and polarized light imaging. NeuroImage. 2017;157:561–574. [PubMed: 28602815]
20. Wang H, Lenglet C, Akkin T. Structure tensor analysis of serial optical coherence scanner images for mapping fiber orientations and tractography in the brain. Journal of Biomedical Optics. 2015;20:036003. [PubMed: 25741662]

21. Lefebvre J, Delafontaine-Martel P, Pouliot P, Girouard H, Descoteaux M, Lesage F. Fully automated dual-resolution serial optical coherence tomography aimed at diffusion MRI validation in whole mouse brains. Neurophotonics. 2018;5:045004. [PubMed: 30681668]
22. Dyrby TB, Søgaard LV, Parker GJ, et al. Validation of in vitro probabilistic tractography. NeuroImage. 2007;37:1267–1277. [PubMed: 17706434]
23. Dauguet J, Peled S, Berezovskii V, et al. Comparison of fiber tracts derived from in-vivo DTI tractography with 3D histological neural tract tracer reconstruction on a macaque brain. NeuroImage. 2007;37:530–538. [PubMed: 17604650]
24. Seehaus AK, Roebroeck A, Chiry O, et al. Histological Validation of DW-MRI Tractography in Human Postmortem Tissue. Cerebral Cortex. 2013;23:442–450. [PubMed: 22345356]
25. Donahue CJ, Sotiropoulos SN, Jbabdi S, et al. Using Diffusion Tractography to Predict Cortical Connection Strength and Distance: A Quantitative Comparison with Tracers in the Monkey. The Journal of neuroscience. 2016;36:6758–70. [PubMed: 27335406]
26. Calabrese E, Badea A, Cofer G, Qi Y, Johnson GA. A Diffusion MRI Tractography Connectome of the Mouse Brain and Comparison with Neuronal Tracer Data. Cerebral Cortex. 2015;25:4628–4637. [PubMed: 26048951]
27. Ourselin S, Bardinet E, Dormont D, et al. Fusion of Histological Sections and MR Images: Towards the Construction of an Atlas of the Human Basal Ganglia. in Medical Image Computing and Computer-Assisted Intervention - MICCAI 2001 (Niessen WJ, Viergever MA, eds.):743–751Springer, Berlin, Heidelberg 2001.
28. Jespersen SN, Leigland LA, Cornea A, Kroenke CD. Determination of Axonal and Dendritic Orientation Distributions Within the Developing Cerebral Cortex by Diffusion Tensor Imaging. IEEE Transactions on Medical Imaging. 2012;31:16–32. [PubMed: 21768045]
29. Foxley S, Sampathkumar V, Andrade VD, et al. Multi-modal imaging of a single postmortem mouse brain over five orders of magnitude of resolution. bioRxiv. 2020:2020.10.07.329789.
30. Tournier JD, Calamante F, Connelly A. MRtrix: Diffusion tractography in crossing fiber regions. International Journal of Imaging Systems and Technology. 2012;22:53–66.
31. Veraart J,Fieremans E,Novikov DS. DiffusionMRInoisemappingusingrandommatrixtheory. Magnetic Resonance in Medicine. 2016;76:1582–1593. [PubMed: 26599599]
32. Veraart J, Novikov DS, Christiaens D, Ades-aron B, Sijbers J, Fieremans E. Denoising of diffusion MRI using random matrix theory. NeuroImage. 2016;142:394–406. [PubMed: 27523449]
33. Tournier JD, Calamante F, Gadian DG, Connelly A. Direct estimation of the fiber orientation density function from diffusion-weighted MRI data using spherical deconvolution. NeuroImage. 2004;23:1176–1185. [PubMed: 15528117]
34. Tournier JD,Calamante F,Connelly A.Robustdeterminationofthefibreorientationdistribution in diffusion MRI: Non-negativity constrained super-resolved spherical deconvolution. NeuroImage. 2007;35:1459–1472. [PubMed: 17379540]
35. Tournier JD, Calamante F, Connelly A. Determination of the appropriate b value and number of gradient directions for high-angular-resolution diffusion-weighted imaging. NMR in Biomedicine. 2013;26:1775–1786. [PubMed: 24038308]
36. Basser PJ, Mattiello J, LeBihan D. MR diffusion tensor spectroscopy and imaging. Biophysical journal. 1994;66:259–67. [PubMed: 8130344]
37. Foxley S, Domowicz M, Karczmar GS, Schwartz N. 3D high spectral and spatial resolution imaging of ex vivo mouse brain. Medical Physics. 2015;42:1463–1472. [PubMed: 25735299]
38. Foxley S, Karczmar GS, Takahashi K. The effects of variations in tissue microstructure from postmortem rat brain on the asymmetry of the water proton resonance. Magnetic Resonance in Medicine. 2018;00:1–11.
39. Mikula S, Binding J, Denk W. Staining and embedding the whole mouse brain for electron microscopy. Nature Methods. 2012;9:1198–1201. [PubMed: 23085613]
40. Mikula S, Denk W. High-resolution whole-brain staining for electron microscopic circuit reconstruction. Nature Methods. 2015;12:541–546. [PubMed: 25867849]
41. Vescovi RF, Cardoso MB, Miqueles EX. Radiography registration for mosaic tomography. Journal of Synchrotron Radiation. 2017;24:686–694. [PubMed: 28452762]

42. Gürsoy D, De Carlo F, Xiao X, Jacobsen C. TomoPy: A framework for the analysis of synchrotron tomographic data. Journal of Synchrotron Radiation. 2014;21:1188–1193. [PubMed: 25178011]
43. Bigun J, Granlund GH. Optimal Orientation Detection of Linear Symmetry. in Proceedings of the IEEE First International Conference On Computer Vision(London):433–438 IEEE 1987.
44. Avants BB, Tustison NJ, Stauffer M, Song G, Wu B, Gee JC. The Insight ToolKit image registration framework. Frontiers in neuroinformatics. 2014;8:44. [PubMed: 24817849]
45. Klein A, Andersson J, Ardekani BA, et al. Evaluation of 14 nonlinear deformation algorithms applied to human brain MRI registration. NeuroImage. 2009;46:786–802. [PubMed: 19195496]
46. Avants BB, Epstein CL, Grossman M, Gee JC. Symmetric diffeomorphic image registration with cross-correlation: evaluating automated labeling of elderly and neurodegenerative brain. Medical image analysis. 2008;12:26–41. [PubMed: 17659998]
47. Raffelt D, Tournier JD, Crozier S, Connelly A, Salvado O. Reorientation of fiber orientation distributions using apodized point spread functions. Magnetic Resonance in Medicine. 2012;67:844–855. [PubMed: 22183751]
48. Raffelt D, Tournier JD, Rose S, et al. Apparent Fibre Density: A novel measure for the analysis of diffusion-weighted magnetic resonance images. NeuroImage. 2012;59:3976–3994. [PubMed: 22036682]
49. Tournier JD, Calamante F, Connelly A. Improved probabilistic streamlines tractography by 2nd order integration over fibre orientation distributions. Proceedings of the International Society for Magnetic Resonance in Medicine. 2010;1670.
50. Ju T, Warren J, Carson J, et al. 3D volume reconstruction of a mouse brain from histological sections using warp filtering. Journal of Neuroscience Methods. 2006;156:84–100. [PubMed: 16580732]
51. Titarenko S, Titarenko V, Kyrieleis A, Withers PJ, IUCr. A priori information in a regularized sinogram-based method for removing ring artefacts in tomography. Journal of Synchrotron Radiation. 2010;17:540–549. [PubMed: 20567087]
52. Titarenko V, IUCr. Analytical formula for two-dimensional ring artefact suppression. Journal of Synchrotron Radiation. 2016;23:1447–1461. [PubMed: 27787251]
53. Prell D, Kyriakou Y, Kalender WA. Comparison of ring artifact correction methods for flat-detector CT. Physics in Medicine and Biology. 2009;54:3881–3895. [PubMed: 19491452]

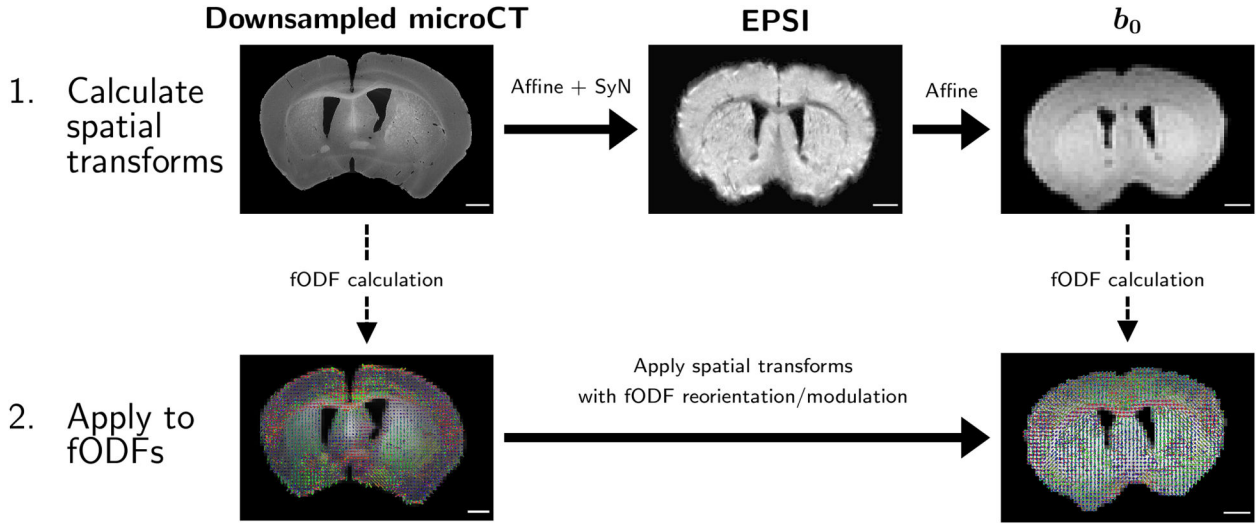

1.

Multi-modal spatial registration pipeline. Downsampled microCT data were registered to EPSI peak-height data using affine and symmetric diffeomorphic (SyN) transforms. EPSI data were registered to the b0 template using affine transforms. The concatenated transforms were then applied to the microCT fODFs calculated at dMRI resolution. Scale bars are 1 mm.

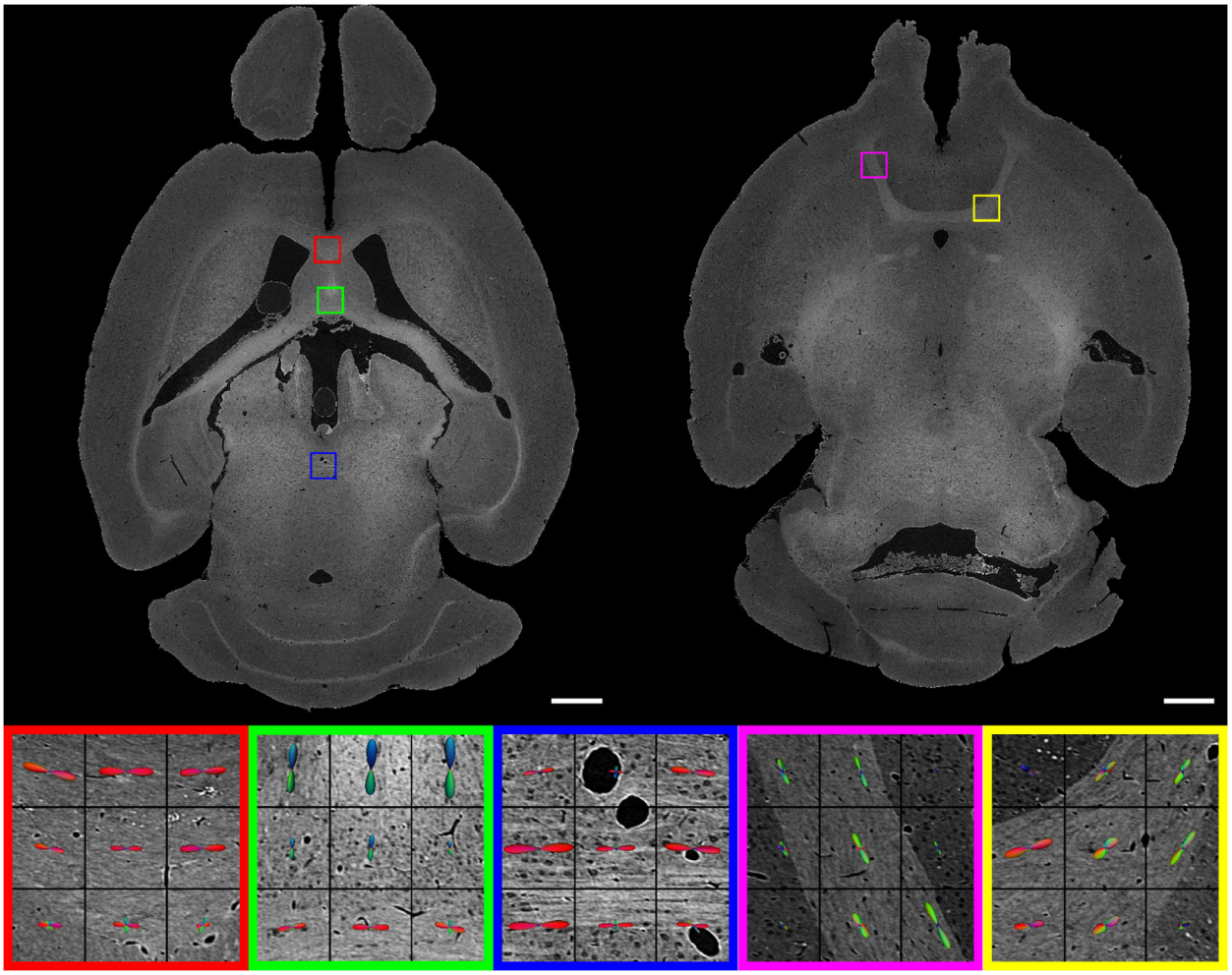

2.

Visualization of microCT data and fODFs across two axial slices. Structure tensor-derived fODFs are visualized as 3D glyphs overlaying ROIs of raw microCT data. Each fODF was calculated from microCT data contained in a 150 μm^3 volume indicated by the black lines. RGB color in the fODFs represents orientation, with red encoding left–right, green encoding anterior–posterior, and blue encoding the superior–inferior direction. Color borders around the ROIs indicate the position of each inset within the whole slices. Scale bars are 1 mm.

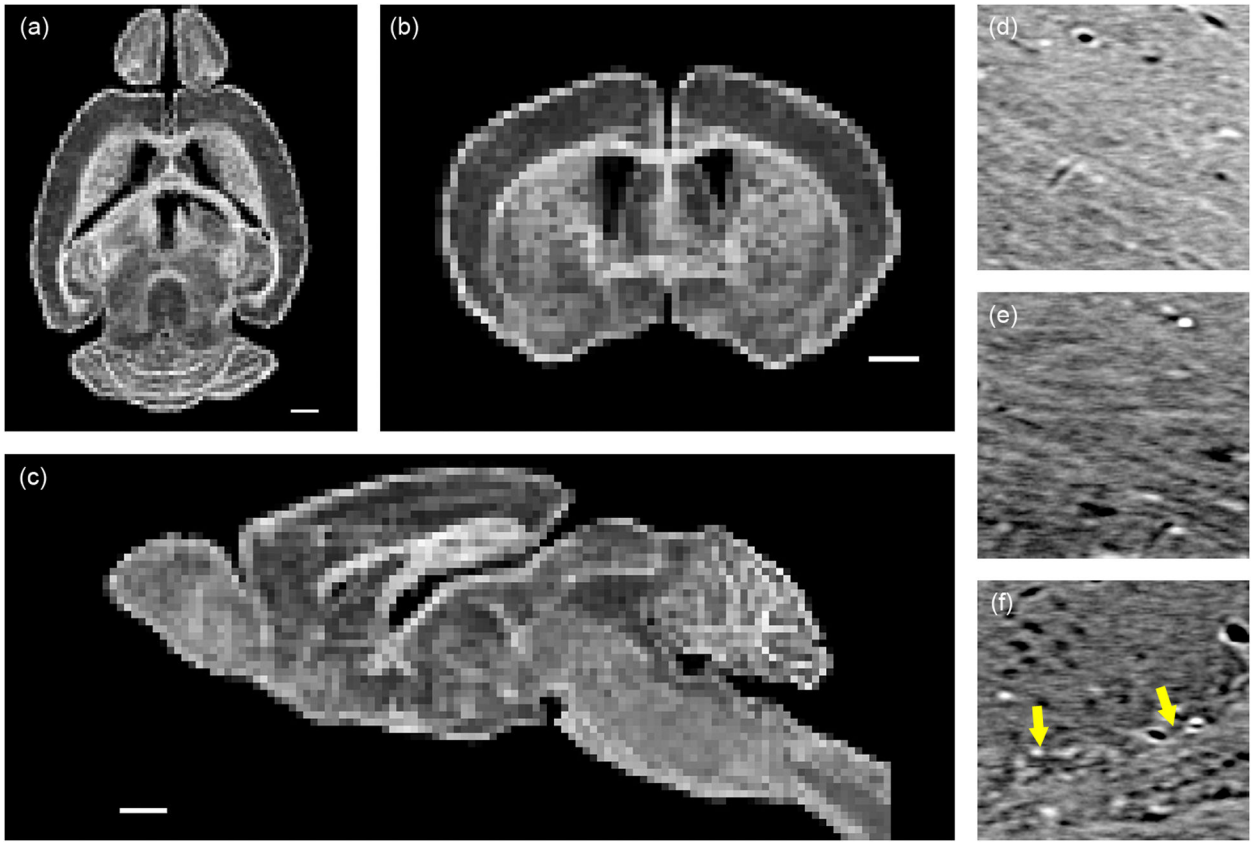

3.

Fiber density measure derived from microCT fODFS. (a-c) Representative FD slices showing contrast between gray and white matter. Scale bars are 1 mm. (d-f) Examples of microCT data from 150 μm^3 cubic regions calculated as having (d) high (FD = 0.41), (e) medium (FD = 0.32), and (f) low (FD = 0.20) fiber density. Arrows in (f) indicate an example of a partial volume effect, where a small region with high fiber density (lower right) is present with a larger region with low fiber density (upper left), resulting in an overall low FD value.

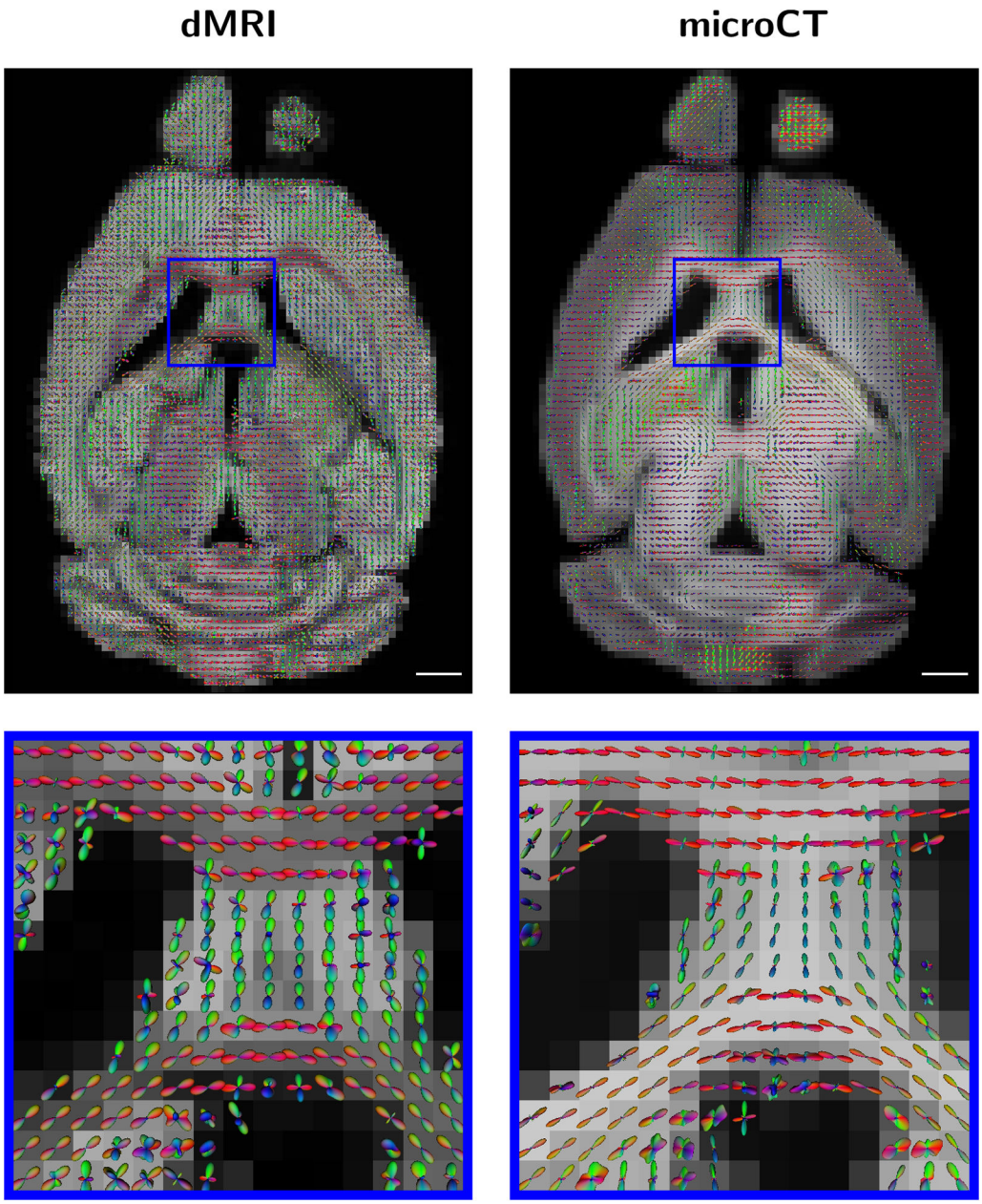

4.

Multi-modal spatial registration. fODFs from both modalities are represented as 3D glyphs overlaying EPSI peak-height data and downsampled microCT data, both spatially aligned to the b_0 of the dMRI dataset. The inset shows the correspondence in fODF shapes along visible fiber tracts. fODFs have been normalized to a maximum value of 1 for visualization. Note that the sharpness of the angular profile of the fODFs differs between the two modalities, resulting from the fact that they have different angular bandlimits ($l_{max} = 4$ and $l_{max} = 8$ for dMRI and microCT, respectively). Scale bars are 1 mm.

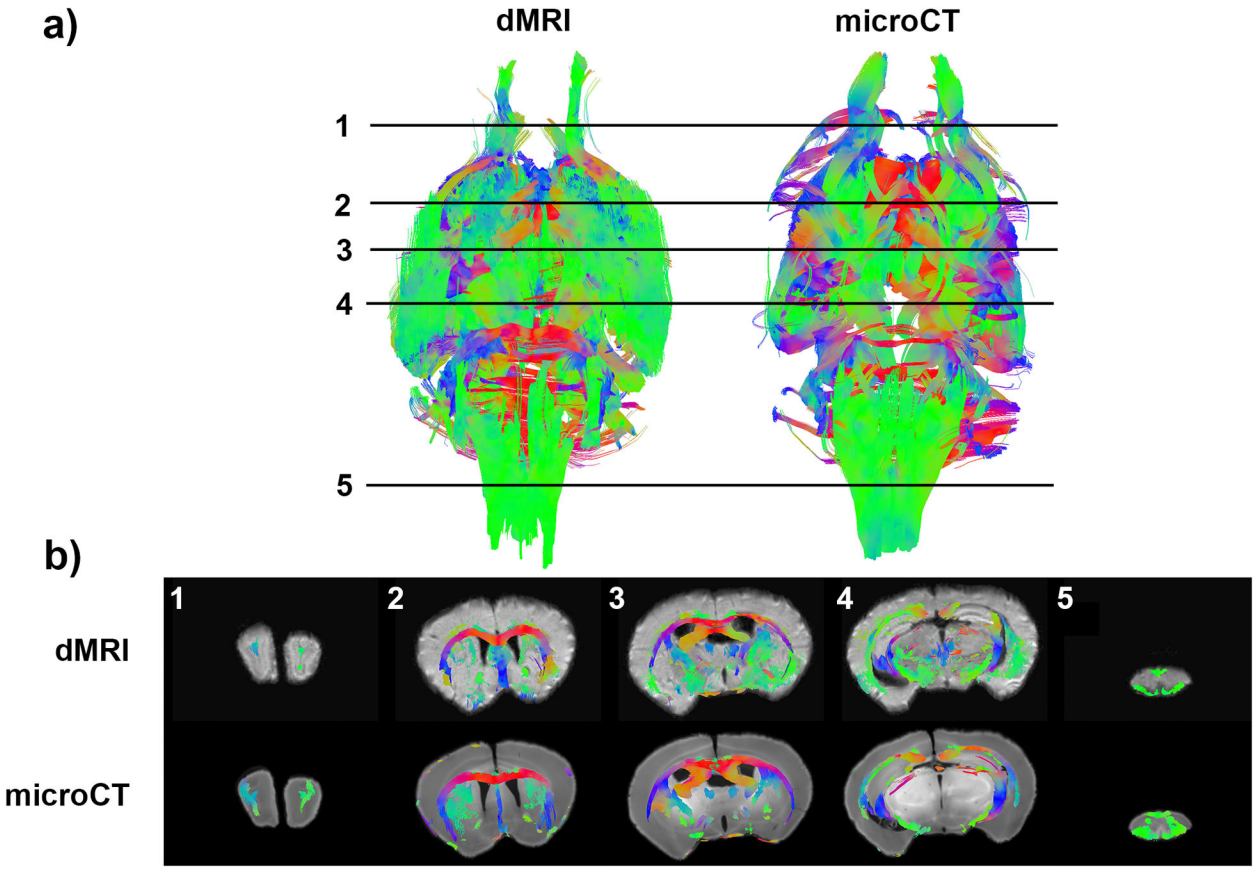

5.

Deterministic tractography results, visualized as streamlines (a) across the whole brain and (b) overlaying five coronal slices of registered dMRI and microCT data, on the top and bottom rows, respectively. Slice numbers in (b) correspond to numbered lines crossing whole-brain results in (a).